Thermally Driven Crossover from Indirect toward Direct Bandgap in 2D Semiconductors: MoSe$_2$ versus MoS$_2$

Sefaattin Tongay,*[†] Jian Zhou,[†] Can Ataca,[‡] Kelvin Lo,[†] Tyler S. Matthews,[†] Jingbo Li,[§] Jeffrey C. Grossman,[‡] and Junqiao Wu*[†,‖]

[†]Department of Materials Science and Engineering, University of California, Berkeley, California 94720, United States

[‡]Department of Materials Science and Engineering, Massachusetts Institute of Technology, Cambridge, Massachusetts 02139, United States

[§]Institute of Semiconductors, Chinese Academy of Sciences, P.O. Box 912, Beijing 100083, People's Republic of China

[‖]Materials Sciences Division, Lawrence Berkeley National Laboratory, Berkeley, California 94720, United States

S Supporting Information

ABSTRACT: Layered semiconductors based on transition-metal chalcogenides usually cross from indirect bandgap in the bulk limit over to direct bandgap in the quantum (2D) limit. Such a crossover can be achieved by peeling off a multilayer sample to a single layer. For exploration of physical behavior and device applications, it is much desired to reversibly modulate such crossover in a multilayer sample. Here we demonstrate that, in a few-layer sample where the indirect bandgap and direct bandgap are nearly degenerate, the temperature rise can effectively drive the system toward the 2D limit by thermally decoupling neighboring layers via interlayer thermal expansion. Such a situation is realized in few-layer MoSe$_2$, which shows stark contrast from the well-explored MoS$_2$ where the indirect and direct bandgaps are far from degenerate. Photoluminescence of few-layer MoSe$_2$ is much enhanced with the temperature rise, much like the way that the photoluminescence is enhanced due to the bandgap crossover going from the bulk to the quantum limit, offering potential applications involving external modulation of optical properties in 2D semiconductors. The direct bandgap of MoSe$_2$, identified at 1.55 eV, may also promise applications in energy conversion involving solar spectrum, as it is close to the optimal bandgap value of single-junction solar cells and photoelechemical devices.

KEYWORDS: 2D-Semiconductors, MoSe$_2$, MoS$_2$, photoluminescence, bandgap, temperature dependence
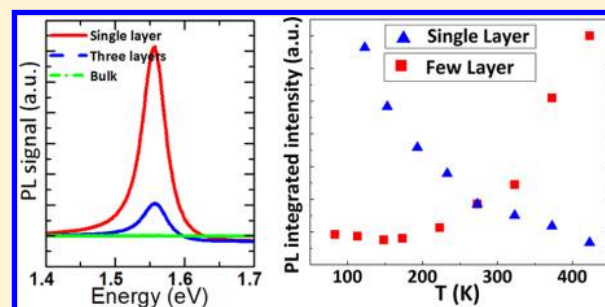
Two-dimensional (2D) materials have attracted much interest mainly owing to their exotic physical properties that are strikingly different from their three-dimensional (bulk) counterparts. Even though graphene, the most famous member of the 2D material family, possesses extraordinary properties[1] and is readily integrated in various applications,[2−4] the lack of a native bandgap in graphene has led to a broad search for other 2D semiconducting materials. More recently, the transition-metal dichalcogenide (TMD) semiconductor MoS$_2$ has been focused on and has shown great potential in the field; single-layer MoS$_2$ has been used as an integral part of transistors,[5−8] sensors,[9] and magnetic materials.[10] However, beyond MoS$_2$, other layered TMDs offer a large variety of 2D materials with distinct properties.

In this work we studied, for the first time, single-layer MoSe$_2$ mechanically exfoliated onto SiO$_2$/Si.[11] Single-layer MoSe$_2$ displays good thermal stability with a 1.55 eV direct bandgap as determined from photoluminescence (PL) measurements. The PL peak intensity is enhanced dramatically from few-layer to single-layer as a result of the crossover from indirect bandgap in the bulk limit to direct bandgap in the quantum (2D) limit,

similar to the behavior of MoS$_2$.[12−14] More interestingly, we find that few-layer MoSe$_2$ flakes posssess a nearly degenerate indirect and direct bandgap, and an increase in temperature can effectively push the system toward the quasi-2D limit by thermally reducing the coupling between the layers. This response in few-layer MoSe$_2$ is similar to the enhancement in PL due to the crossover from indirect to direct bandgap originating from the quantum confinement effect. In this regard, MoSe$_2$ shows stark differences from MoS$_2$ where not only the bandgap value is higher than in MoSe$_2$, but also the indirect and direct bandgaps are well-separated in energy and hence far from degenerate. Our results not only introduce single-layer MoSe$_2$ as a new 2D material with a bandgap well matched to the solar spectrum, but also open up a new direction for 2D applications where external modulation of bandgap and optical properties is desired.
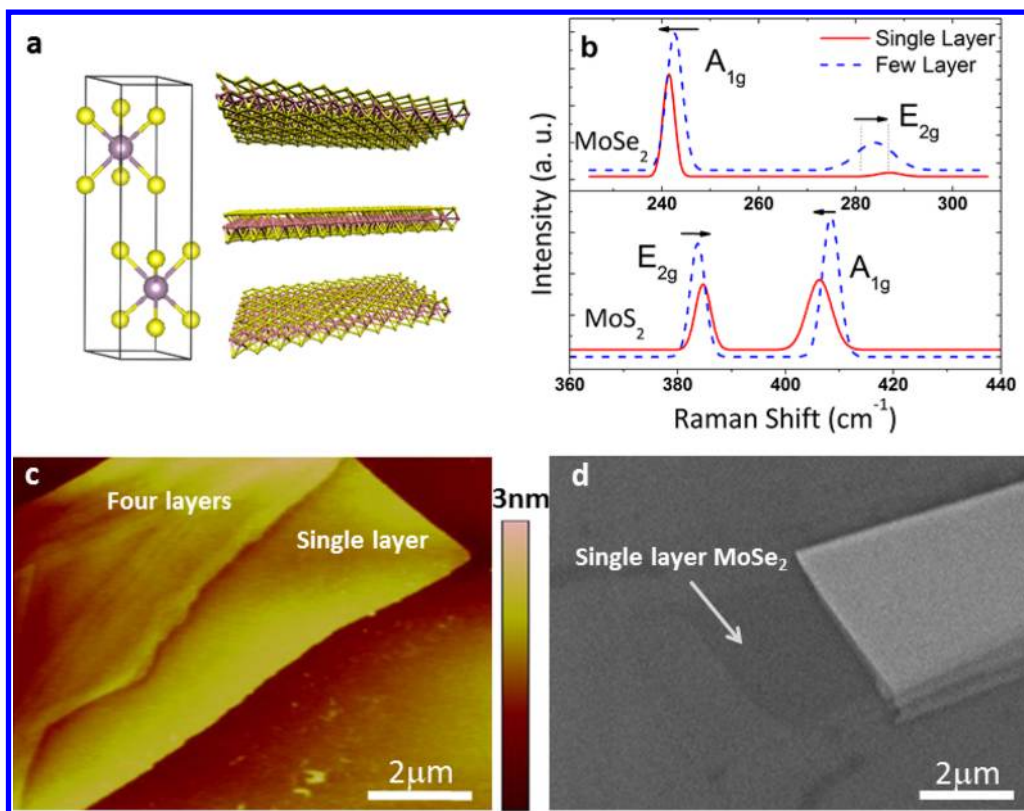
Figure 1. (a) Crystal structure of $MoSe_2$ in the bulk ($2H$-$MoSe_2$). (b) Raman spectrum of single (solid red line) and more than 10 layers (dashed blue line) MoX_2 (X = S, Se). (c) AFM image taken on a single-layer $MoSe_2$ flake. (d) SEM image taken on a $MoSe_2$ flake.

Single and few-layer MoS_2 and $MoSe_2$ flakes were exfoliated from bulk MoS_2 and $MoSe_2$ crystals onto 90 nm SiO_2/Si substrates using a conventional mechanical exfoliation technique[11] (see Supporting Information). 90 nm SiO_2/Si substrates allowed us to improve the contrast between MoX_2 (X = S, Se) layers and at the same time increased the visibility of the single layer sheets.[15] Exfoliated few-layer flakes have shown characteristic A_{1g} (out-of-plane) and E_{2g}^1 (in-plane) Raman modes (Figure 1b) located at 243.0 and 283.7 cm^{-1} for $MoSe_2$ and 408.7 and 383.7 cm^{-1} for MoS_2. For $MoSe_2$, the A_{1g} mode is at a higher frequency than E_{2g} mode, consistent with earlier studies.[16−18] We find that the peak position of these Raman modes show a slight dependence on the layer thickness. In the single layer limit, the A_{1g} Raman mode softens to 241.2 (406.1) cm^{-1} as the E_{2g}^1 mode stiffens to 287.3 (384.7) cm^{-1} for $MoSe_2$ (MoS_2). Since interlayer coupling is absent in the single layer limit, the out-of-plane A_{1g} mode is expected to soften as a result of reduction of the restoring forces arising from the absence of interlayer coupling. However this model does not account for the stiffening of the in-plane E_{2g}^1 mode.[19] More interestingly, the intensity ratio between the A_{1g} and E_{2g}^1 modes ($I_{A_{1g}}/I_{E_{2g}^1}$) changes from 4.9 for few-layer (∼10 layers) to 23.1 for the single-layer $MoSe_2$, while the ratio remains nearly a constant (∼1.2) in the MoS_2 case. In Figure 1c−d, we display AFM and SEM images taken on a single-layer $MoSe_2$. The single layers typically display 0.9−1 nm thickness in the AFM contact mode, and the surface is free of residues. Also, these single layers are readily visible on 90 nm SiO_2/Si under the scanning electron microscope as shown in Figure 1d.

In the bulk limit, $MoSe_2$ is an indirect bandgap semiconductor with a 1.1 eV bandgap value,[20] and therefore the bandgap PL is expected to be rather weak. However, the few-layer $MoSe_2$ flakes show gradual enhancement in PL intensity at around 1.5−1.6 eV, and the PL peak intensity reaches its maximum value for a single-layer $MoSe_2$ as shown in Figure 2a. Similar to this observation, enhancement in PL for single-layer
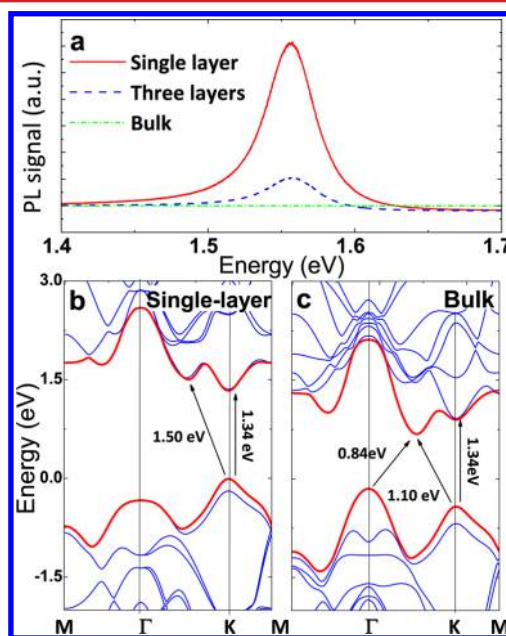
Figure 2. (a) Measured room-temperature photoluminescence on a single-layer (red), three-layer (blue dashed), and bulk (green dotted dashed) $MoSe_2$. Here the measurement parameters including laser excitation intensity are the same. (b−c) Calculated band structure of single-layer and bulk $MoSe_2$.

MoS_2 has been observed previously[12−14] and attributed to an indirect-to-direct bandgap crossover associated with the quantum confinement in the perpendicular direction.[13] To confirm this, we compute the electronic band structure of single-layer $MoSe_2$ and bulk $MoSe_2$ in Figure 2b−c calculated by generalized gradient approximatio (GGA) + van der Waals (vdW) + spin−orbit density functional theory (see Supporting Information, Figure 3a−b). Here, three-dimensional MoX_2
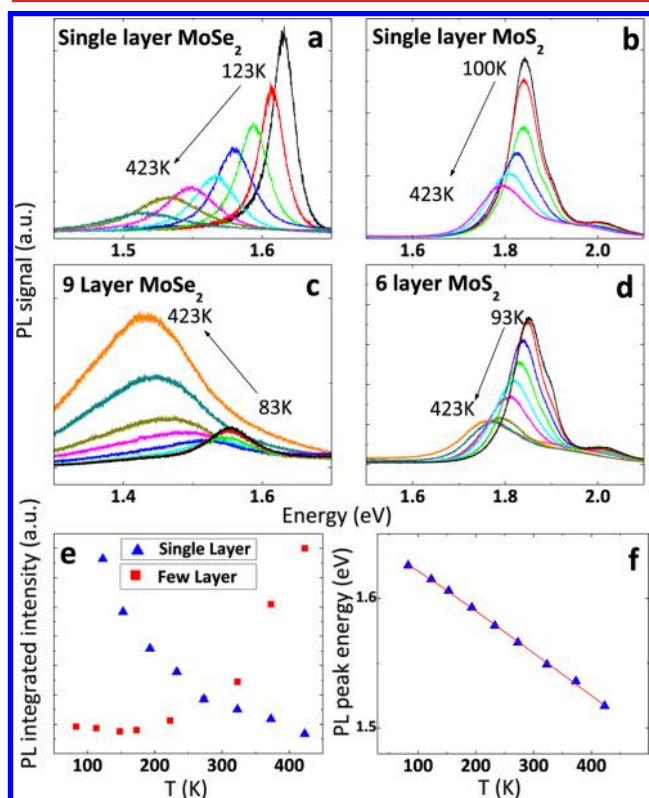
Figure 3. Temperature dependence of photoluminescence on (a−b) single-layer $MoSe_2$ and MoS_2 and (c−d) few-layer $MoSe_2$ and MoS_2. Here, the PL intensity ratio between the single-layer and few-layer MoX_2 typically reaches 50−500. (e) Temperature dependence of photoluminescence intensity measured on a single-layer (blue triangles) and nine-layer (red squares) $MoSe_2$ flakes. (f) Variation of the single-layer $MoSe_2$ bandgap values (PL peak energy) in the 87−450 K range. The red line shows the fitting results using 1.

$(2H-MoX_2)$ possesses both time-reversal and inversion symmetry, and therefore spin-up and spin-down valence bands are degenerate. Upon lowering the dimensionality of the system to single layer (1H-), the inversion symmetry is lost, and the degeneracy is lifted due to spin−orbit interaction. It is therefore necessary to take into account the spin−orbit coupling interaction in density functional theory (DFT) calculations to determine the accurate band structure. We also note that the first principles calculations typically underestimate the actual bandgap, leading to small discrepancies from the experimental values. In accord with the above discussions, bulk $MoSe_2$ displays 0.84 eV Γ to Γ−K, 1.10 eV K to Γ−K an indirect bandgaps, and a 1.34 eV K−K direct bandgap (Figure 2c). In contrast, for single-layer $MoSe_2$, Γ to Γ−K and K to Γ−K increases, while the K−K direct gap remains nearly unchanged and $MoSe_2$ becomes a direct bandgap semiconductor with a 1.34 eV bandgap value at the K symmetry point (Figure 2b). Even though the band structure

calculations explain the enhancement in PL in the quantum confinement limit, it does not address the origin of the weaker PL peak observed for few-layer flakes. In fact, our calculations show that two and three layer $MoSe_2$ have an indirect bandgap but with almost degenerate direct and indirect bandgap values (Figure 4a−b).[21] In such a case, hot carriers are expected to transiently occupy the available states around the K symmetry point and result in hot PL although with weaker intensity compared to the single layer case (Figure 2a). This hot PL model was invoked and justified by Mak et al.[13] to explain the weak PL in few-layer MoS_2. The hot PL effect is expected to be stronger in $MoSe_2$ due to the closer values of direct and indirect bandgaps.

Before presenting striking differences between single and few-layer $MoSe_2$ and MoS_2, we emphasize that the bandgap (PL peak position) of single-layer $MoSe_2$ is located at 1.55 eV, where this value is near 1.9 eV for single-layer MoS_2. Moreover, heating single-layer $MoSe_2$ in air to 500 K, the maximum temperature that can be attained in our system, does not alter its PL peak intensity and position upon cooling back to room temperature, implying that the single layers are thermally stable up to these temperatures. Previously, the oxidization characteristics of bulk MoS_2 and $MoSe_2$ have been studied, and they were found to be oxidized in the 500−700 K range.[22,23] However, considering that the studied flakes are two-dimensional, the observed stability is surprising. This might be due to self-limited oxidation and merits further studies. The observed bandgap value is significantly smaller than that of MoS_2, and this not only extends the bandgap values observed in 2D semiconductors but also points to creating a range of bandgap values by alloying 2D semiconductors. More importantly, the 1.55 eV direct bandgap in $MoSe_2$ is more relevant to device applications involving the solar spectrum, as it is near the optimal bandgap value for single-junction solar cells and photoelectrochemical cells.

Next, we turn our attention to the temperature dependence of PL measured on single- and few-layer samples of $MoSe_2$ and MoS_2 (Figure 3a−d). Such measurements not only yield the bandgap dependence on temperature but also allow us to understand the physical mechanism that governs the light emission process. Before discussing the effect of temperature on the bandgap (E_g), we focus on the change in PL intensity as a function of temperature. As seen in Figure 3a−c, the temperature dependence of PL intensity of the single-layer and few-layer $MoSe_2$ show striking differences. While the PL intensity is much reduced at high temperatures for single-layer $MoSe_2$, it is surprisingly enhanced for few-layer $MoSe_2$. Generally the PL of semiconductors decreases in intensity as the PL peak broadens with increasing temperature. The suppression in PL intensity and peak broadening are typically attributed to the exponential enhancement in nonradiative electron−hole recombination processes, reducing the probability of radiative transition. Even though this model applies well to single-layer $MoSe_2$, it fails for the few-layer $MoSe_2$ samples where the PL intensity is enhanced at high temperatures (see Figure 3e, red squares). We also employed similar measurements on a single-layer and few-layer MoS_2 flakes in the same temperature window, and we have found that the PL intensity of MoS_2 decreases at high temperatures regardless of the layer thickness (Figure 3b and d)[24] just like in the case of single-layer $MoSe_2$ and other conventional semiconductors. The distinct difference in the temperature

behavior of these two materials points out to intrinsic differences in their band structure.

To gain further insight, we compare the band structures of MoSe$_2$ and MoS$_2$ from bulk to few-layer and to the single-layer limit. According to our DFT calculations as well as previously reported studies on MoSe$_2$ and MoS$_2$,[21,25] these two materials possess indirect bandgap in bulk and become direct bandgap in the 2D limit. Therefore in those limits, one would expect MoSe$_2$ and MoS$_2$ to behave similarly. However, we find that the rate of the indirect-to-direct bandgap crossover differs significantly between MoS$_2$ and MoSe$_2$. Even though single-layer MoSe$_2$ is a direct bandgap semiconductor (1.34 eV), the indirect bandgap value (1.50 eV) lies close to the direct bandgap. This difference of 0.16 eV is much smaller than the difference of 0.35 eV between the direct (1.54 eV) and indirect (1.89 eV) bandgap of single-layer MoS$_2$. As the number of layers increases, the quantum confinement in the perpendicular direction is relaxed, and therefore the indirect bandgap value becomes smaller, while the direct bandgap value remains largely unchanged, due mostly to the heavier effective mass associated with the K symmetry point (see Supporting Information, Figures 3 and 4). During this crossover the direct and indirect gaps in the case of bilayer and few-layer MoSe$_2$ becomes nearly degenerate. An increase in temperature slightly expands the interlayer distance as evidenced by the temperature-dependent Raman measurements (see Supporting Information) and tends to decouple neighboring MoSe$_2$ layers, pushing the system further toward the bandgap degeneracy. In this case, the contribution from the hot PL across the direct bandgap to the PL intensity becomes much stronger at high temperatures without any need for a phonon-assisted process. The abnormal increase in PL intensity at high temperatures, on the other hand, cannot be attributed to Boltzmann tailing of equilibrium electrons populating the conduction and valence bands at the K point where the direct bandgap occurs. This is because this K point bandgap is still 0.18 eV above the indirect bandgap which is much larger than k_BT. In a 3D semiconductor with similar band configuration, Ge, the direct bandgap is 0.14 eV above the indirect bandgap, but such an unusual PL behavior as in MoSe$_2$ has never been observed in Ge. This contrast highlights the uniqueness of 2D semiconductors that they support a high-efficiency hot PL process.

Shown in Figure 4 is the calculated bandgap crossover of few-layer MoSe$_2$ MoS$_2$ as a function of modulation in interlayer distance. Here, the relaxed equilibrium position is fixed to zero, and additional layer spacing (abscissa) imitates the effect of temperature rise on the interlayer coupling. As seen from the figure, at the equilibrium, the indirect bandgap (Γ to Γ−K) defines the fundamental bandgap but is close in value to the direct band (K to K). Increasing the interlayer spacing reduces the coupling between the layers and leads to an increase in Γ to Γ−K gap, while the direct gap K−K remains unchanged. During this transition, the indirect and direct bandgaps in bilayer and trilayer MoSe$_2$ would become degenerate as discussed above. For larger interlayer spacing, the coupling would be weakened to a point that individual layers in the few-layer system start to behave as single layers with a 1.34 eV direct bandgap. On the contrary, since the indirect and direct gaps are well-separated in the bilayer MoS$_2$, band degeneracy cannot be thermally approached unless the layers are physically decoupled from each other. This distinct difference between these two similar materials leads to a drastic difference in the temperature dependence of their PL intensity.
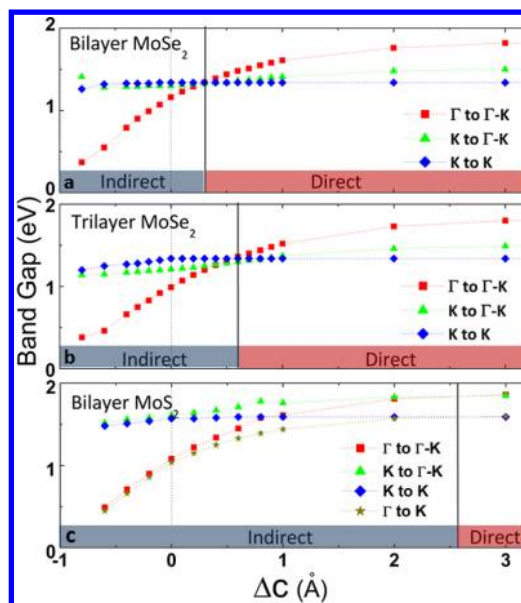
Figure 4. Variation of the bandgap values between different symmetry points as a function of layer spacing on (a) bilayer MoSe$_2$, (b) trilayer MoSe$_2$, and (c) bilayer MoS$_2$. A fully relaxed (equilibrium) position is fixed to zero, and additional layer spacing (abscissa) imitates the effect of temperature on the interlayer coupling.

Since this is the first experimental observation of single-layer MoSe$_2$, for completeness, we discuss the effect of temperature on the bandgap (PL peak position) of the single-layer MoSe$_2$. In Figure 3f, we show the temperature dependence of the bandgap extracted out from Figure 3a. The observed decrease in the bandgap as a function of temperature is very similar to that observed in conventional semiconductors where such a decrease at higher temperatures due to increased electron−phonon interactions as well as slight changes in the bonding length.[26] Even though the origin of the temperature dependence in E$_g$ is known, a physically meaningful and accurate formula of $E_g(T)$ is lacking. Often times, the temperature dependence is fitted by the empirical Varshni relation[27] where the parameters lack clear physical meaning. Here, we employ a semiempirical fitting function;[28]

$$E_g(T) = E_g^0 - S\langle\hbar\omega\rangle[\cosh(\langle\hbar\omega\rangle/2k_BT) - 1] \qquad (1)$$

where E_g^0 is the zero-temperature bandgap value, S is a parameter describing the strength of the electron−phonon coupling, $\langle\hbar\omega\rangle$ is the average acoustic phonon energy involving in the electron−phonon interaction, and last the cosh term is related to the density of phonons at the specific temperature. We find that this model fits the temperature dependence of the bandgap well as shown in Figure 3f with E_g^0 = 1.64 eV, S = 1.93, and $\langle\hbar\omega\rangle \geq 11.6$ meV (93 cm^{-1}). In comparison, similar fitting to single-layer MoS$_2$ yields E_g^0 = 1.86 eV, S = 1.82, and $\langle\hbar\omega\rangle$ = 22.5 meV (182 cm^{-1}).

To summarize, we have experimentally shown the first optical emission studies of single-layer and few-layer MoSe$_2$ semiconductors. While single-layer MoSe$_2$ possesses a direct bandgap, in the few-layer limit the indirect and direct bandgap are nearly degenerate. As a result, we find that this system can be effectively driven toward the 2D limit by thermally decoupling neighboring layers via interlayer thermal expansion. This finding leads to an enhancement in photoluminescence of few-layer MoSe$_2$ at high temperatures, similar to the enhance-

ment of photoluminescence due to the bandgap crossover going from the bulk to the quantum limit. However, observed temperature dependence of the PL in few-layer $MoSe_2$ is strikingly different from the well-explored MoS_2 where the indirect and direct bandgaps are far from degenerate. This effect points to potential applications involving external modulation of optical properties in 2D semiconductors.

Methods. *Experimental Details.* Raman and photoluminescence measurements were performed using a Renishaw Raman system with 488 nm laser in combination with commercially available liquid N_2 cooling stage. Typically, samples were measured using 100× lens, and the laser beam was focused on a ~1 μm diameter spot. Atomic force microscopy measurements were performed using a commercial system (Multimode, Veeco). The imaging and thickness measurements have been done with both contact mode and tapping mode.

See Supporting Information for the $MoSe_2$ single crystal growth process. MoS_2 single crystals were purchased from SPI Inc. and 2Dsemiconductors.com. See the Supporting Information for more on sample preperation.

Density Functional Theory Calculations. Our calculations are based on first-principles density functional theory (DFT) using projector augmented wave potentials.[29] The exchange correlation potential has been represented by the generalized gradient approximation characterized by Perdew–Burke–Ernzerhof[30] including van der Waals (vdW) corrections[31] both for spin-polarized and spin-unpolarized cases. Effects of spin–orbit coupling and noncollinear magnetism are taken into account in the spin-polarized calculations. The supercell size, kinetic energy cutoff, and Brillouin zone (BZ) sampling of the calculations have been determined after extensive convergence analyses. A large spacing of ~15 Å between 2D single layers is used to prevent interlayer interactions. A plane-wave basis set with kinetic energy cutoff of 300 eV is used. In the self-consistent field potential and total energy calculations the BZ is sampled by special **k**-points. The numbers of these **k**-points are $(25 \times 25 \times 1)$ and $(15 \times 15 \times 5)$ for the primitive $1H-MoS_2$ and $2H-MoS_2$ unit cell and are scaled according to the size of the super cells. All atomic positions and lattice constants are optimized using the conjugate gradient method, where the total energy and atomic forces are minimized. The convergence for energy is chosen as 10^{-6} eV between two consecutive steps, and the maximum Hellmann–Feynman forces acting on each atom is less than 0.01 eV/Å upon ionic relaxation. The pressure in the unit cell is kept below 5 kbar. Numerical calculations have been performed by using VASP software.[32] Frequencies of phonon modes are calculated using small displacement method $(SDM)^{33}$ in terms of forces calculated from first-principles.

ASSOCIATED CONTENT

ⓢ Supporting Information

Sample preparation methods and additional information on the DFT calculations and Raman peaks. This material is available free of charge via the Internet at http://pubs.acs.org.

AUTHOR INFORMATION

Corresponding Author

*E-mail: tongay@berkeley.edu; wuj@berkeley.edu.

Notes

The authors declare no competing financial interest.

REFERENCES

(1) Castro Neto, A. H.; Guinea, F.; Peres, N. M. R.; Novoselov, K. S.; Geim, A. K. *Rev. Mod. Phys.* **2009**, *81*, 109−162.

(2) Wu, Y.; Lin, Y. M.; Bol, A. A.; Jenkins, K. A.; Xia, F.; Farmer, D. B.; Zhu, Y.; Avouris, P. *Nature* **2011**, *472*, 74−78.

(3) Miao, X.; Tongay, S.; Petterson, M. K.; Berke, K.; Rinzler, A. G.; Appleton, B. R.; Hebard, A. F. *Nano Lett.* **2012**, *12*, 2745−2750.

(4) Zhang, B.; Cui, T. *Appl. Phys. Lett.* **2011**, *98*, 073116.

(5) Radisavljevic, B.; Radenovic, A.; Brivio, J.; Giacometti, V.; Kis, A. *Nat. Nanotechnol.* **2011**, *6*, 147−150.

(6) Zhang, Y.; Ye, J.; Matsuhashi, Y.; Iwasa, Y. *Nano Lett.* **2012**, *12*, 1136−1140.

(7) Lui, H.; Ye, P. *IEEE Electron Device Lett.* **2012**, *33*, 546−548.

(8) Yin, Z.; Li, H.; Li, H.; Jiang, L.; Shi, Y.; Sun, Y.; Lu, G.; Zhang, Q.; Chen, X.; Zhang, H. *ACS Nano* **2012**, *6*, 74−80.

(9) Li, H.; Yin, Z.; He, Q.; Li, H.; Huang, X.; Lu, G.; Fam, D. W. H.; Tok, A. I. Y.; Zhang, Q.; Zhang, H. *Small* **2012**, *8*, 63−67.

(10) Tongay, S.; Varnoosfaderan, S. S.; B. R. Appleton, J. W.; Hebard, A. F. *Appl. Phys. Lett.* **2012**, *101*, 123105.

(11) Novoselov, K. S.; Geim, A. K.; Morozov, S. V.; Jiang, D.; Zhang, Y.; Dubonos, S. V. *Science* **2004**, *306*, 666−669.

(12) Splendiani, A.; Sun, L.; Zhang, Y.; Li, T.; Kim, J.; Chim, C.-Y.; Galli, G.; Wang, F. *Nano Lett.* **2010**, *10*, 1271−1275 ; PMID: 20229981.

(13) Mak, K. F.; Lee, C.; Hone, J.; Shan, J.; Heinz, T. F. *Phys. Rev. Lett.* **2010**, *105*, 136805.

(14) Eda, G.; Yamaguchi, H.; Voiry, D.; Fujita, T.; Chen, M.; Chhowalla, M. *Nano Lett.* **2011**, *11*, 5111−5116.

(15) Benameur, M. M.; Radisavljevic, B.; Sahoo, J. S. H.; Berger, H.; Kis, A. *Nanotechnology* **2011**, *22*, 125706.

(16) Sugai, S.; Ueda, T. *Phys. Rev. B* **1982**, *26*, 6554.

(17) Lee, C.; Yan, H.; Brus, L. E.; Heinz, T. F.; Hone, J.; Ryu, S. *ACS Nano* **2010**, *4*, 2695−2700 ; PMID: 20392077.

(18) Sekine, T.; Izumi, M.; Nakashizu, T.; Uchinokura, K.; Matsuura, E. *J. Phys. Soc. Jpn.* **1980**, *49*, 1069−1077.

(19) Chakraborty, B.; Bera, A.; Muthu, D. V. S.; Bhowmick, S.; Waghmare, U. V.; Sood, A. K. *Phys. Rev. B* **2012**, *85*, 161403.

(20) Scheer, R.; Schock, H.-W. *Chalcogenide Photovoltaics: Physics, Technologies, and Thin Film Devices*; Wiley-VCH Verlag GmbH & Co.: Weinheim, Germany, 2011.

(21) Yun, W. S.; Han, S. W.; Hong, S. C.; Kim, I. G.; Lee, J. D. *Phys. Rev. B* **2012**, *85*, 033305.

(22) Moore, G. D. *ASLE Trans.* **1970**, *13* (2), 117−126.

(23) Lavik, M. T.; M., G. D.; Medved, T. M. *ASLE Trans.* **1968**, *11*, 44−55.

(24) Korn, T.; Heydrich, S.; Hirmer, M.; Schmutzler, J.; Schuller, C. *Appl. Phys. Lett.* **2011**, *99*, 102109.

(25) Ataca, C.; Sahin, H.; Ciraci, S. *J. Phys. Chem. C* **2012**, *116*, 8983−8999.

(26) Yu, P.; Cardona, M. *Fundamentals of Semiconductors: Physics and Materials Properties*; Springer: New York, 1999.

(27) Sze, S. M. *Physics of Semiconductor Devices*; John Wiley and Sons: New York, 1981.

(28) O'Donnell, K. P.; Chen, X. *Appl. Phys. Lett.* **1991**, *58*, 2924−2926.

(29) Blöchl, P. E. *Phys. Rev. B* **1994**, *50*, 17953−17979.

(30) Perdew, J. P.; Burke, K.; Ernzerhof, M. *Phys. Rev. Lett.* **1996**, *77*, 3865−3868.

(31) Grimme, S. *J. Comput. Chem.* **2006**, *27*, 1787.

(32) Kresse, G.; Hafner, J. *Phys. Rev. B* **1993**, *47*, 558−561.

(33) Alfe, D. *Phys. Commun.* **2009**, *180*, 2622.

Supplementary Information for Thermally driven crossover from indirect toward direct bandgap in 2D semiconductors: MoSe$_2$ versus MoS$_2$

Sefaatin Tongay,[*],[†] Jian Zhou,[†] Can Ataca,[*],[‡] Kelvin Lo,[†] Tyler S. Matthews,[†] Jingbo Li,[¶] Jeffrey C. Grossman,[‡] and Junqiao Wu[*],[†],[§]

Department of Materials Science and Engineering, University of California, Berkeley, CA 94720, United States, Department of Materials Science and Engineering, Massachusetts Institute of Technology, Cambridge, MA, 02139, United States, Institute of Semiconductors,Chinese Academy of Sciences, PO Box 912, Beijing 100083, People's Republic of China, and Materials Sciences Division, Lawrence Berkeley National Laboratory, Berkeley, California 94720, United States

E-mail: tongay@berkeley.edu; ataca@mit.edu; wuj@berkeley.edu

---

[*]To whom correspondence should be addressed

[†]Department of Materials Science and Engineering, University of California, Berkeley, CA 94720, United States

[‡]Department of Materials Science and Engineering, Massachusetts Institute of Technology, Cambridge, MA, 02139, United States

[¶]Institute of Semiconductors,Chinese Academy of Sciences, PO Box 912, Beijing 100083, People's Republic of China

[§]Materials Sciences Division, Lawrence Berkeley National Laboratory, Berkeley, California 94720, United States

Synthesis of Single-layer MoX$_2$

Even though mechanical exfoliation technique is widely used to transfer single layer graphene from graphite onto Si/SiO$_2$, exfoliating other layered materials is not trivial. The difficulty to obtain single layers of other layered materials comes from the fact that (i) while the interlayer coupling is at most 100meV in graphene, this value is around 150-220 meV depending on the choice of material, making the exfoliation more diffucult comparing to graphene, (ii) currently laboratory grown highly oriented pyrolitic graphite (HOPG) is widely studied, available, and possesses large grain sizes. On the contrary, other layered materials are rather rare in nature, and are typically disordered, preventing us to exfoliate large area single-layers. Despite such difficulties, various techniques can be used to improve the single-layer yield after exfoliation. Before describing these techniques, we briefly present our typical exfoliation process: We first press Nitto Denko Inc (3193MS) or 3M Magic tape uniformly onto the single-crystal flakes and remove the tape, leaving very thin flakes transferred onto the tape. After this step, we press tape/MoX$_2$ (X=S, Se) evenly from the top onto the substrate (90nm SiO$_2$/Si from MTI Inc Item number: SI-SO-Ba100D05C1-90nm with less than 0.5nm surface roughness) and peel it off from one side to another with approximately 0.5mm/s rate. This process leaves mostly few-layer flakes deposited onto the thermal oxide and finding single layers requires careful sample examination under the optical microscope (typically single layers are light gray color on 90nm SiO$_2$). Additionally, Raman spectroscopy (the peaks positions are different for few-layer and single layer flakes), photoluminescence (note: only single layers yield high PL intensity and therefore can be used as a tool to find single layered flakes), and AFM measurements allow us to identify the single layer flakes.

In this study, we use the following techniques to improve our yield; (1) Freshly cleaved surfaces increases the single-layer yield: We believe that this is related to the larger number of (slightly) decoupled layers soon after fresh exfoliation. Once the surface is pressed onto Si/SiO2 surface and cleaved, the single-layers couple back to the MoX$_2$ bulk crystals. Once the cleaved surface is pressed onto the substrate, we cleave the surface (MoX$_2$ / Tape) again before the next exfoliation. (2) Choice of tape: We observe that using 3193MS (single-sided), 120°C release temperature,

7.2N/mm from Nitto Denko Inc. yields larger area and glue-free single-layer materials. However, the yield rate is typically low (1 out of 3 samples). Use of 3M magic tape brand single sided tape give higher yields but the flakes are typically 1-3microns and mostly contain glue (either at the edge, under the flake, or near the flake). (3) Cleavage speed: After pressing the tape evenly from the top on the substrate, we try to cleave the tape slowly. We notice that this typically improves the flake size. On the contrary, fast cleavage yields smaller flakes. (4) Applied pressure during the transfer: Applying high pressure to the tape on the substrate typically leaves glue-residues around the flake. However, if no pressure is applied, slightly decoupled single-layers (on the freshly cleaved surface) do not adhere to the substrate which reduces the transfer rate. (5) Quality of the starting material: We believe that the above techniques can be applied to $MoSe_2$ (or any other layered material) powder with big grain sizes. However, in this study the $MoSe_2$ (or any MX_2) crystals were grown by the well established direct vapor transport technique (DVT) using Br_2 as a transport agent. The details were given elsewhere in numerous publications.[1–3] More specifically, prior to the crystal growth, quartz ampules ($\sim$2cm in diamater and 20cm long) were cleaned using acetone, isopropanol, and methanol. After the cleaning, the quartz ampule was annealed at 450°C for 3 hours for degassing. The quartz ampule containing Br_2 ($\sim$4-6mg/cm^3) and the elements in stoichiometric proportions (%99.99 Mo and Se powders from Sigma Aldrich) were sealed at 10^{-6} Torr and all the powders were collected on one side of the ampule. The quartz ampule was loaded into the three-zone furnace and the side with the powder was kept at 800°C (the other end was at 900°C to avoid powder transport) for a day for pre-reaction. After this step, the powder side of ampule was gradually heated up to 950°C ($\sim$5°C/min ramp rate and the other end was kept at 920°C for a day for the crystal growth. After the growth, dark black, shiny, graphite-like single-crystal pieces / flakes were collected in quartz ampule. Typical flakes were 4mmx4mm in size and 50μm in thickness. X-ray diffraction (XRD) data taken on the $MoSe_2$ show strong and sharp (002), (004), and (006) peaks indicating that the flakes are highly crystalline and are layered (Figure 1). The data match the JCPDS 15-0029 entry for 2H-$MoSe_2$, and are consistent with the independent Raman spectrum measurements. MoS_2 pieces were purchased from SPI lab supplies Inc. and were

cleaved continuously till fresh and clean surfaces were exposed. (6) Substrate surface quality: We find that any residue on the Si/SiO_2 surface reduces the yield rate mainly due to the lack of enough coupling between the substrate and the flake. Cleaning the SiO_2 surfaces using piranha solution for a minute improves the yield rate.
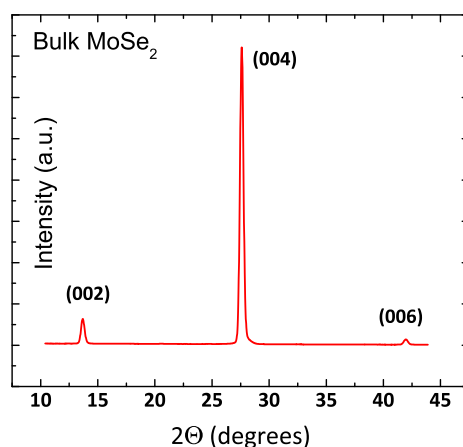

Figure 1: X-ray diffraction (XRD) data taken on the 2H-$MoSe_2$ flakes. The 2H-$MoSe_2$ flakes show high crystallinity as evidenced by the sharp and strong (002), (004), and (006) peaks.

Temperature Dependence of $MoSe_2$ Raman Peaks

In the manuscript, we argue that an increase in temperature slightly expands the interlayer distance and tends to decouple neighboring $MoSe_2$ layers, pushing the system further toward the bandgap degeneracy. As a result of this, the PL intensity becomes much stronger. To elucidate this point, we provide temperature dependent Raman measurements on few-layer $MoSe_2$. We first note that the out-of-plane A_{1g} mode is expected to soften as a result of reduction of the restoring forces arising from the decrease in interlayer coupling. This is similar to softening of the A_{1g} mode from bulk to single-layer limit where the interlayer coupling becomes absent. In Figure 2(a-b), we show temperature dependence of the A_{1g} mode from 423K down to 83K. As the temperature increases,

A$_{1g}$ mode softens (shifts to the lower wavenumber). The softening in the Raman peak position is consistent with the interlayer decoupling mentioned in this work and provides a direct evidence for the increase in interlayer distance and reduction in the interlayer coupling. To present more quantitative analysis, we calculate the c-axis lattice contant at different temperatures using the out-of-plane linear expansion coefficient for bulk (few-layer) MoSe$_2$ ($\alpha_{c-axis}\sim$1.29$\cdot$10^{-5}K^{-1})[4] and room temperature c-axis lattice constant ($c\sim$1.2935 nm)[4] via c(T)=c(300K)+$\alpha_{c-axis}\cdot c$(300K)$\cdot$(T-300K). Next, we plot the out-of-plane (A$_{1g}$) Raman peak position for few-layer MoSe$_2$ measured at different temperatures versus the calculated c-axis lattice contant values at the same temperature (Figure 2(c)). This figure allows us to correlate the Raman peak position to the lattice constant and in the limit where the few layer MoSe$_2$ A$_{1g}$ peak position converges to the room temperature single layer A$_{1g}$ peak position. In this limit, each layer can be pictured as if it is a single layer decoupled from adjacent layers. Following Figure 2(c), we observe that few-layer MoSe$_2$ flake already reaches the forementioned limit at 423K, consistent with our interpretations in the manuscript and the supplementary. Here, we note that one would expect to reach the truly single-layer limit at temperatures much higher than 423K. However, since the single-layer in our experiment is still coupled to the thermal oxide substrate (as opposed to being suspended), the A$_{1g}$ Raman peak is stiffened (therefore the A$_{1g}$ peak position is higher than that of truly independent single layer.

Density Functional Theory Calculations: Quantum Confinement Effect

Up until now most of the theoretical works on MoX$_2$ (X=chalcogen atom: O, S, Se, Te) dominated by nonmagnetic ground states.[5-13] Three dimensional (2H-) MoX$_2$ lattice structure has D6h group symmetry which includes time-reversal and inversion symmetry. These result in degenerate
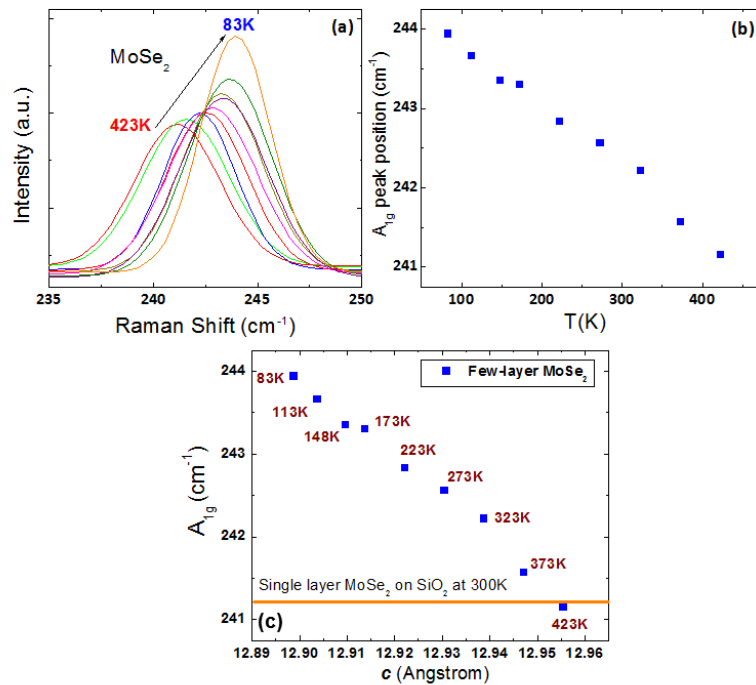
Figure 2: (a) Temperature dependence of the out-of-plane (A_{1g}) Raman peak in few-layer $MoSe_2$. (b) The change in the A_{1g} peak position as a function of temperature. (c) Measured A_{1g} versus calculated c-axis lattice constant graph for few-layer $MoSe_2$ flakes. The orange straight line shows the A_{1g} peak position for single layer $MoSe_2$ flake on 90 nm thermal oxide at room temperature.
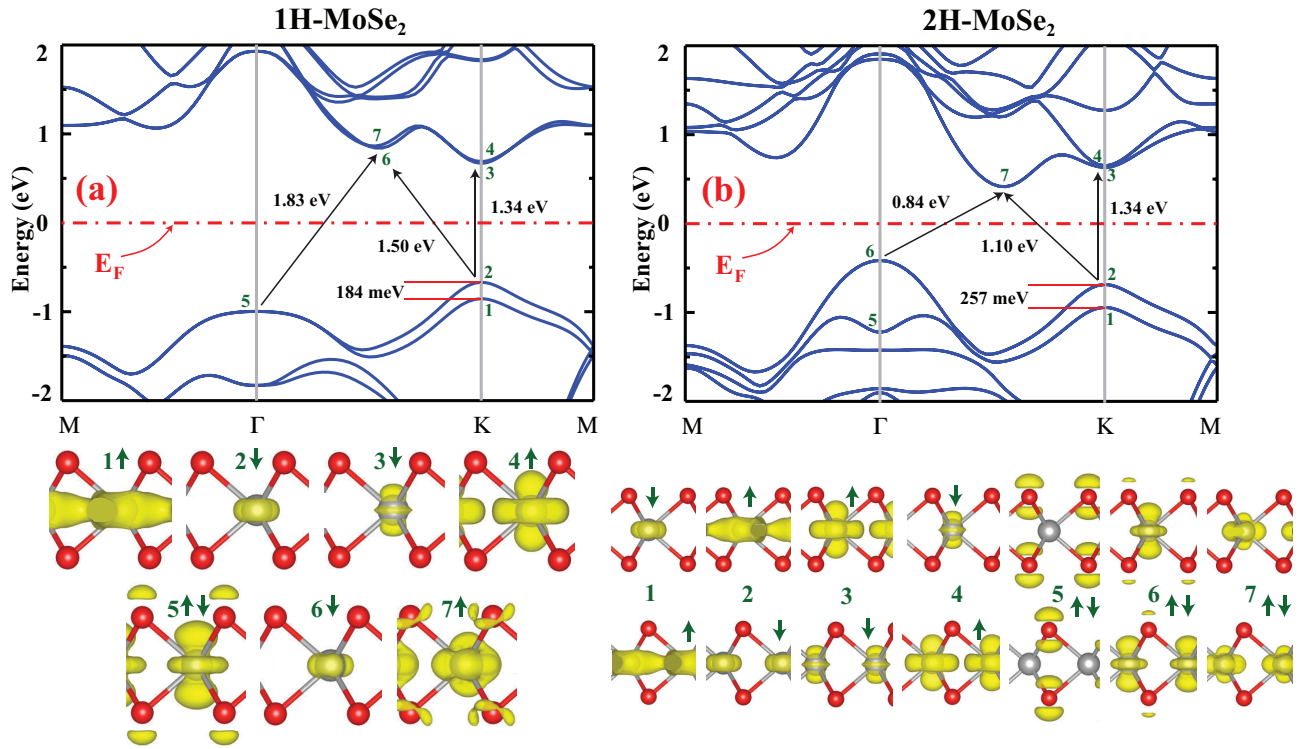
Figure 3: (a) Calculated energy band structures, and state charge densities of single layer MoSe$_2$. (1H-MoSe$_2$) Upper panel is the energy band structure along the $M - \Gamma - K - M$ directions of Brillouin zone. The zero of energy is set at the Fermi level, E_F, shown by red dashed dotted line. Energy difference between specific points are indicated by arrows. Lower panels are isosurface charge densities of the specific states at certain k-points indicated by numerals. Isosurface value is taken as 5×10^{-5} electrons/Å^3. Spin character of each isosurfaces are indicated by $\uparrow$, $\downarrow$ or $\uparrow\downarrow$ respresenting spin-up, spin-down or degenerate spin states, respectively. (b) Similar to (a), but bulk MoSe$_2$ is considered. (2H-MoSe$_2$)

spin-up and spin-down bands. Lowering the dimensionality of the system to single layer (1H-) MoX$_2$ having D3h group symmetry and which is not inversion symmetric, the degeneracy of spin-up and spin-down bands split at special k-points due to spin-orbit interaction.[14,15]

Interaction between layers of transition-metal dichalcogenides is dominated from van der Waals (vdW) interaction.[7] In order to find the accurate lattice structure of 2H-MoSe$_2$ and 2H-MoS$_2$, one has to include effects of vdW in the density fuctional theory (DFT) calculations. Recent study[7] showed that Grimme's method[16] for inclusion of vdW effects in DFT calculations would result in lattice constants of 2H-MoS$_2$ very close to experimental values. For this reason in all of DFT calculations in this paper Grimme's method is used as vdW interaction functional. Spin-orbit interaction and noncollinear magnetism effects are also taken into account to understand the differences in energy band structures between weakly interacting bulk (2H-) and single layer (1H-) MoS$_2$ and MoSe$_2$. Spin-orbit interaction plays a crutial role in the electronic structure, however noncollinear magnetism is not observed in DFT calculations. The calculated lattice parameters for single layer and bulk MoSe$_2$ (MoS$_2$) are $a = 3.320$ ($a = 3.19$) and $a = 3.317$, $c = 13.02$ ($a = 3.19$, $c = 12.34$) which is very close to the experimental parameters ($a = 3.282, c = 12.948$ for 2H-MoSe$_2$[17] and $a = 3.16$, $c = 12.30$ for 2H-MoS$_2$[18]) respectively.

In Supplementary Figure 3, the energy band structure of 1H- and 2H-MoSe$_2$ are shown with band decomposed charge densities at certain **k**-points. In DFT calculations excluding the spin-orbit interaction spin-up and spin-down valance bands of 1H-MoSe$_2$ around **K**-point are degenerate. However as a result of spin-orbit interaction, spin-up and spin-down bands marked as '1' and '2' in Supplemeneraty Figure 3(a) split from each other by 184 meV. (The splitting is 149 meV for 1H-MoS$_2$) These bands are dominated from Mo atoms d$_{x^2-y^2}$ and d$_{xy}$ orbitals. In the case of 2H-MoSe$_2$ the contribution of the bands do not change as shown in the partial charge densities marked as '1' and '2' in Supplementary Figure 3(b). However one MoSe$_2$ layer has spin-up and neighboring MoSe$_2$ layer has spin-down charge. The spin splitting does not affect the conduction band edge at **K** point which are only from Mo atoms' d$_{z^2}$ orbitals for both single layer and bulk MoSe$_2$ indicated as '3' and '4' in Supplementary Figure 3(a) and (b). Absence of contribution of

charge form chalcogen atoms (Se and S) at **K** point, one may assume that the layer-layer interaction does not influece the direct gap at **K**-point. To test this assumption the electronic band structre of 2, 3, 5, and 7 layers of MoSe$_2$ and MoS$_2$ are calculated. The direct band gap at K-points does not alter as the number of transtion metal dichalcogenide layers changes as shown in Supplementary Figure 4.
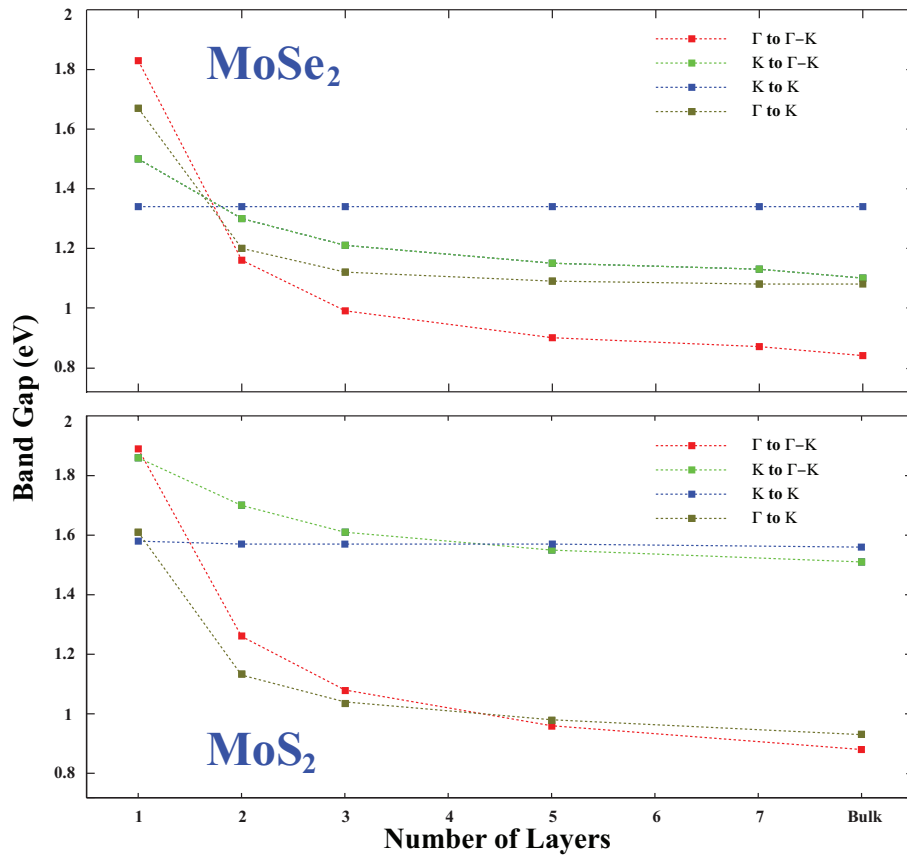

Figure 4: Variation of the band gap values between different symmetry points as a function of number of layers for MoSe$_2$ and MoS$_2$.

Dimensionality effects in electronic structure play an important role at valance band around Γ-point and conduction band in $\Gamma - K$ direction. At Γ point, valance band edge is a combination of Mo atoms' d$_{z^2}$ orbitals and Se (S) atoms' p$_z$ orbitals shown as '5' and '6' for 1H-MoSe$_2$ and 2H-MoSe$_2$ in Supplementary Figure 3, respectively. Positively charged transition metal atoms

are sandwiched between negatively charged chalcogen atoms.[6,8] Due to coulombic repulsion of negative charges between layers, chalcogen atoms' p_z orbital contribution in 2H-MoX$_2$ are lower than that of 1H-MoX$_2$. Conduction band edge in $\Gamma - K$ direction are governed by Mo atoms' d$_{xy}$, d$_{x^2-y^2}$ and X atoms p orbitals for both monolayer and bulk MoX$_2$ structures. Spin-splitting due to spin-orbit interaction in 1H-MoX$_2$ is diminished for the bulk structure. (See isosurface charges '6' and '7' in Supplementary Figure 3(a) and '7' in Supplementary Figure 3(b).) The absence of repulsive coulomb and attractive van der waals interaction in monolayer MoX$_2$ lead to an increase in the indirect gap between Γ and $\Gamma - K$ points. Similar observations are also carried on 2, 3, 5, and 7 layers of MoX$_2$, and observed that as the number of layers increase, the value of the indirect gap decreases and changes the electronic structure from direct band to indirect band gap semiconductor as shown in Supplementary Figure 4.

Finite Temperature Effects in DFT calculations

In order to take into account the temperature dependence in DFT calculations, one can start with the temperature dependence of the lattice parameters. Taking into account the quasi-harmonic approximation, one can write the Helmholtz free energy as:

$$F(V,T) = E_{DFT} + F_{harmonic}(V,T) \tag{1}$$

$$F_{harmonic} = k_B T \int_0^\infty g(w) ln(2 sinh(\hbar w)/2k_B T) dw \tag{2}$$

where the first term in Eqn. 1 is the ground state energy calculated using DFT. The second term is vibrational energy contribution to the free energy. Configurational effects are excluded, since there is no change in the geometric structure. The vibrational contribution is calculated by summing the phonon modes over the wavevectors in the Brillouin Zone. This is treated in $g(w)$, the phonon density of states, in Eqn. 2. The effect of the anharmonicity in the lattice energy is included by letting the phonon frequencies to depend on the lattice parameters. Hence, the recepie

we follow is to start with the geometry optimization of the structure. We then calculated the phonon spectrum of the structure with DFT using Small Displacement Method.[19] Phonon calculation using DFT including spin-orbit interactin is computationally expensive and demanding tasks. For this reason, we then expanded the lattice structure by 0.1% and calculated ground state energy and phonon spectrum again. We iteratively expanded the lattice constant until 1.5%. Using Eqn. 1 and 2, we calculated the temperature and lattice constant dependent free energy of the system. In Supplementary Figure 5, variation of lattice constants of 2H-MoSe$_2$ with respect to temperature (vertical expansion) is indicated. Due to finite expansion step size, we fitted our results to a second order equation, $p_1 T^2 + p_2 x + p_3$, which resulted in the lowest RMS error ($\sim 10^{-4}$) to find the linear thermal expansion coefficient, $\alpha = p_2/p_3$. The calculated values are in close agreement with experimental values for bulk MoS$_2$ and MoSe$_2$.[4]

To understand how the temperature affects the layer-layer seperation, we started with calculating the thermal expansion coefficient of 2H-MoS$_2$ and MoSe$_2$ in the vertical direction. (the direction perpendicular to the plane of 2D MoX$_2$ as shown in Supplementary Figure 5(a)). We first note that the expansion coefficient is higher for MoSe$_2$ compared to MoS$_2$ and therefore MoSe$_2$ interlayer separation increases faster with temperature thanthat of MoS$_2$. Moreover, considering that the direct and indirect bandgap values are closer in energy in MoSe$_2$ (comparing to MoS$_2$), the band structure of MoSe$_2$ becomes more temperature dependent. As a result, even though linear thermal expansion coefficient of 2H-MoSe$_2$ is only slightly ($\sim 20\%$) larger than that of 2H-MoS$_2$, the effect of temperature on the MoSe$_2$ electronic structure is more dramatic. More specifically, the value of the indirect-gap (Γ to Γ-K) increases much more than that of 2H-MoS$_2$, and MoSe$_2$ become more degenerate at higher temperatures while this effect is negligible in the bulk MoS$_2$. Here, we also note that the observed changes in bulk MoSe$_2$ will be amplified for few-layer MoSe$_2$, as indirect and direct bandgap values are even closer in energy (comparing to the bulk MoSe$_2$), making it easier to achieve degeneracy at higher temperatures.
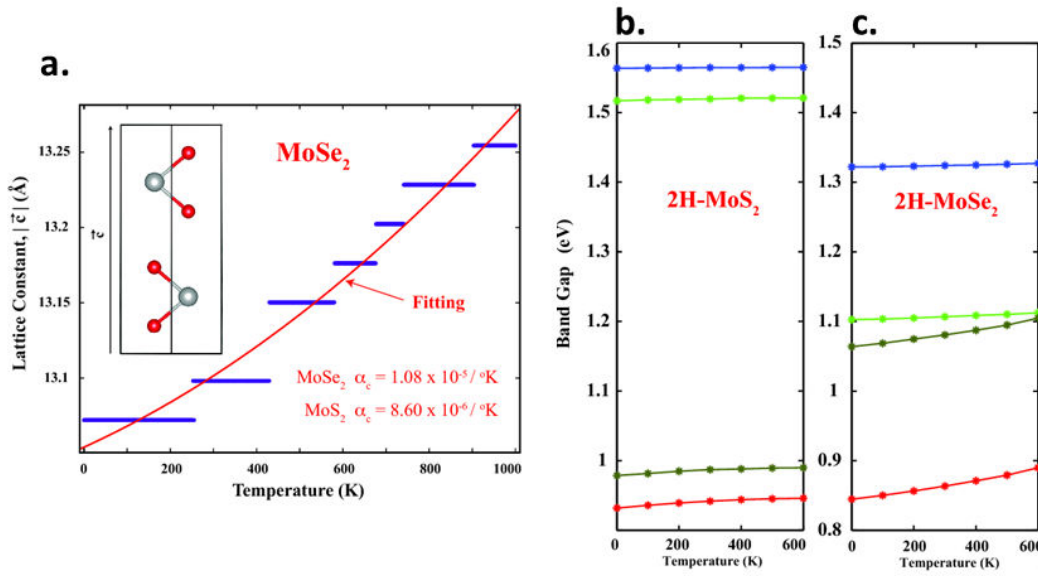
Figure 5: (a) Temperature dependance of the lattice constants in vertical direction *c* is considered for 2H-MoS$_2$ and MoSe$_2$. Purple line segments are calculated data and red lines are the fitting. Linear thermal expansion coefficients and variation of band gaps with respect to temperature of (b) 2H-MoS$_2$ and (c) 2H-MoSe$_2$ are also shown.

The effects of thermal expansion in few layer systems are expected to be different due to the lack of strong van der Waals interaction in the surface layers. In order to model few layer structures, we used temperature dependent ab-inito molecular dynamics (MD) calculations. The time steps were taken to be $2\text{x}10^{-15}$ s and the velocities of the atoms were normalized every 40 steps. For both bilayer and trilayer $MoSe_2$, we carried out six sequential MD calculations. Each calculations are 2500 time-steps long, modelling 5 pico seconds. Sequential calculations are: increasing the temperature from 0 to 150 K, constant temperature at 150 K, increasing the temperature from 150 to 300 K, constant temperature at 300 K, increasing the temperature from 300 to 450 K and constant temperature at 450 K. At every constant temperature calculations (150, 300, 450 K), we determined the average $MoSe_2$ layer-layer distance. For trilayer (bilayer) $MoSe_2$ the average layer-layer distances are 0.16 (0.45) Angstrom, 0.25 (0.58) Angstrom and 0.50 (0.90) Angstrom for 150K, 300K and 450 K, respectively. As the number of layers in the structure decreases from bulk to two, the effects of temperature in the layer-layer spacing is more dramatic. As shown in Figure 4 in the manuscript, bilayer $MoSe_2$ will be a direct-gap material even at temperatures lower than 150 K. However trilayer $MoSe_2$ will turn into a direct-gap material at temperatures higher than 450 K. In $2H-MoSe_2$ the change in the layer-layer distance with varying temperature is not much due to strong van der Waals interaction. Even at 450 K, the layers are seperated by ~ 0.07 Angstrom more than that of 0K. However, the modification in the electronic structure is notable.

References

(1) Hu, S.; Liang, C.; Tiong, K.; Huang, Y. *Journal of Alloys and Compounds* **2007**, *442*, 249–251.

(2) Agarwal, M.; Patel, P.; Gupta, S. *Journal of Crystal Growth* **1993**, *129*, 559 – 562.

(3) Hicks, W. T. *J. Electrochem. Soc.* **1964**, *111*, 1058–1065.

(4) El-Mahalawy, S. H.; Evans, B. L. *Journal of Applied Crystallography* **1976**, *9*, 403–406.

(5) Ataca, C.; Sahin, H.; Akturk, E.; Ciraci, S. *JOURNAL OF PHYSICAL CHEMISTRY C* **2011**, *115*, 3934–3941.

(6) Ataca, C.; Ciraci, S. *JOURNAL OF PHYSICAL CHEMISTRY C* **2011**, *115*, 13303–13311.

(7) Ataca, C.; Topsakal, M.; Akturk, E.; Ciraci, S. *JOURNAL OF PHYSICAL CHEMISTRY C* **2011**, *115*, 16354–16361.

(8) Ataca, C.; Sahin, H.; Ciraci, S. *The Journal of Physical Chemistry C* **2012**, *116*, 8983–8999.

(9) Ataca, C.; Ciraci, S. *Phys. Rev. B* **2012**, *85*, 195410.

(10) Cahangirov, S.; Ataca, C.; Topsakal, M.; Sahin, H.; Ciraci, S. *Phys. Rev. Lett.* **2012**, *108*, 126103.

(11) Mak, K. F.; Lee, C.; Hone, J.; Shan, J.; Heinz, T. F. *PHYSICAL REVIEW LETTERS* **2010**, *105*, 136805.

(12) Li, T.; Galli, G. *JOURNAL OF PHYSICAL CHEMISTRY C* **2007**, *111*, 16192–16196.

(13) Splendiani, A.; Sun, L.; Zhang, Y.; Li, T.; Kim, J.; Chim, C.-Y.; Galli, G.; Wang, F. *Nano Letters* **2010**, *10*, 1271–1275, PMID: 20229981.

(14) Zhu, Z. Y.; Cheng, Y. C.; Schwingenschlögl, U. *Phys. Rev. B* **2011**, *84*, 153402.

(15) Xiao, D.; Liu, G.-B.; Feng, W.; Xu, X.; Yao, W. *Phys. Rev. Lett.* **2012**, *108*, 196802.

(16) Grimme, S. *JOURNAL OF COMPUTATIONAL CHEMISTRY* **2006**, *27*, 1787–1799.

(17) Morales, J.; Santos, J.; Tirado, J. *SOLID STATE IONICS* **1996**, *83*, 57–64.

(18) Böker, T.; Severin, R.; Müller, A.; Janowitz, C.; Manzke, R.; Voß, D.; Krüger, P.; Mazur, A.; Pollmann, J. *Phys. Rev. B* **2001**, *64*, 235305.

(19) Alfe, D. *COMPUTER PHYSICS COMMUNICATIONS* **2009**, *180*, 2622–2633.